DOI: ADD DOINUMBER HERE

DSMC-based Correction Factor for Low-fidelity Hypersonic Aerodynamics of Re-entering Objects and Space Debris

Alessandro Falchi[a], Edmondo Minisci[a†], Massimiliano Vasile[a], Davide Rastelli[b], and Niccolò Bellini[b]

[a]*Aerospace Centre of Excellence (ACE) - University of Strathclyde*
James Weir Building, 75 Montrose St, Glasgow G1 1XQ, UK
{alessandro.falchi, edmondo.minisci, massimiliano.vasile}@strath.ac.uk

[b]*Space Mind Division - New Production Concept S.r.l.*
Via Errico Malatesta 27/29, Imola (BO) 40026, Italy
{d.rastelli, n.bellini}@npcitaly.com

[†]Corresponding author

Abstract

This work investigates the differences between hypersonic aerodynamic coefficients computed with two different tools, having two different levels of fidelity: a high fidelity code implementing the Direct Simulation Monte Carlo method and a low fidelity one based on the approximated hypersonic local surface inclination technique. Different multivariate correction factors to reduce the low-fidelity tool error have been defined using a High Dimensional Model Representation algorithm. The low fidelity approach with the implemented correction factor has been tested on different space objects, the Gravity field and steady-state Ocean Circulation Explorer satellite and a 3U CubeSat with a deployed drag sail; the results are presented and commented.

1. Introduction

Hypersonic Aerodynamic analyses have a central role for the design of spacecraft and spaceplanes, but are also crucial to study the atmospheric re-entry of any space object that could potentially impact the Earth, as well as the orbit propagation and end-of-life assessments of satellites in Low Earth Orbits (LEOs). Many low-fidelity software codes have been developed within the framework of re-entry and survivability analysis to save computational costs and time, each having a lookup table for average aerodynamic coefficients or its own aerodynamic module that may work with a three degree-of-freedom (DoF) or 6DoF approach.

Different tools can be used for evaluating a re-entry scenario. A distinction is made between object and spacecraft oriented tools;[8] the first ones include Debris Assessment Software[17] (DAS) developed by NASA, the tool uses a constant C_D assumed to be 2.2. The framework developed by ESA: Debris Risk Assessment and Mitigation Analysis[9] (DRAMA) which uses the Spacecraft Entry Survival Analysis Module (SESAM) to perform the re-entry simulation employing an averaged random tumbling aerodynamic C_D and assumes the lift to drag ratio to be zero. Another proprietary tool developed by the NASA is ORSAT,[18,19] which uses a random tumbling C_D estimated for different attitude motions and objects, based on a 3DoF equations of motion propagation. Yet among the object oriented tools there is DEBRISK,[16] after the initial breakup triggered at 78km the simple-shaped objects are simulated using a 3DoF trajectory propagation, the aerodynamics are dependent on the shape, attitude and flow conditions. The first developed spacecraft oriented tool is the Spacecraft Atmospheric Reentry and Aerothermal Breakup[5] (SCARAB), currently used by the European Space Agency, which uses a local panel inclination method for assessing the aerodynamics in a 6DoF trajectory propagation, simulating the spacecraft or satellite as close to the reality as possible. A newly developed spacecraft/object oriented re-entry tool is the Simplified Aerothermal Model[13] (SAM) which employs a local panel inclination method for computing the spacecraft aerodynamics. SAM uses a 6DoF trajectory propagation on the entire spacecraft before the break-up and a 3DoF propagation on the "fragments" afterwards. All these tools have a very simplified aerodynamic approach, which could lead to non-quantified uncertainty in the re-entry impact footprint area and position estimation.

This work presents the recent improvements of the Free Open Source Tool for Re-entry of Asteroids and Debris[10] (FOSTRAD), developed at the University of Strathclyde. The software is based on the local surface inclination method,

and can perform aerodynamic and aero-thermodynamic analyses from the free molecular (FM) flow to the continuum regime. The study presented here focuses on FOSTRAD's aerodynamics module.

FOSTRAD's aerodynamics module shows a good agreement with experimental data when applied to blunt-shaped bodies,[12] but when applied to sharp-edged bodies like parallelepiped and flat cylinders (with the length parallel to the flow direction) it presents a decreased accuracy. A recent investigation[2] on the Gravity field and steady-state Ocean Circulation Explorer satellite aerodynamics (GOCE, Figure 16), which is characterized by sharp edges and a high lateral to frontal surface ratio, has highlighted that FOSTRAD underestimates the C_D from -30 to +5%. The tool shows the maximum error when the flow is parallel to the longitudinal axis. From a re-entry analysis perspective, the attitude-dependent error is the reason for an increased uncertainty when the software is used for performing re-entry trajectory propagations or uncertainty quantifications, even though a lesser impact would be noticed when performing a re-entry with a random tumbling assumption. Moreover, the aerodynamic uncertainty can be directly connected with an increased uncertainty in the probable impact ground footprint of a re-entry scenario. In addition, as the tool can also be used for spacecraft and satellites design optimization, this kind of error could greatly affect the result of the shape optimization preliminary design. Therefore, it is of utmost importance correcting and reducing the hypersonic aerodynamic attitude-dependent error.

In this work, a surrogate model (SM) of an attitude-dependent correction factor (C_F, Eq. 1) for parameterized primitive shapes has been defined (Section 5). The C_F is based in the FM flow regime and therefore influences the aerodynamics also in the rarefied transitional regime. The C_F has been computed by coupling FOSTRAD, a high-fidelity Direct Simulation Monte Carlo (DSMC - dsmcFoam[21]) and an Adaptive Derivative High Dimensional Model Representation-based algorithm[6] (AD-HDMR).

$$C_F = \frac{C_{D,DSMC}}{C_{D,FOSTRAD}} \tag{1}$$

where $C_{D,DSMC}$ and $C_{D,FOSTRAD}$ are representative of the chosen aerodynamic coefficient (drag) computed with the DSMC and FOSTRAD respectively. A different SM will be generated for each parameterized shape: parallelepipeds, and cylinders. A particular geometrical parametrization has been chosen: the frontal area to total area ratio. This specific parametrization allows the SMs to be used independently from the absolute dimension, which could grant their general implementation within FOSTRAD depending on the analyzed shape similarity wrt the simulated geometries. The particular parallelepiped parametrization is suitable also for CubeSats. A particular 3U CubeSat study case with and without drag sail has been thoroughly analyzed (Section 6.2). The defined cylindrical C_F model has been tested also on GOCE aerodynamics (Section 6.3), where its application has shown a sensible error reduction on the estimated drag.

2. Direct Simulation Monte Carlo

The DSMC software that has been used in the current work is the dsmcFoam solver developed by Scanlon et ali.[20,21] The DSMC method allows to resolve steady and unsteady flow fields within the FM flow and rarefied transitional regime by simulating the statistical collisions among particles and object surfaces. Provided enough computational power, it would also be usable to model the continuum regime.

This work has been focused on the FM regime, where the inter-particles collisions are unlikely to occur. In the FM flow an inter particles collision-less model is able to properly represent the flow field, as indeed only the collisions with the object walls are evaluated. The method allows the computation of the macroscopic properties by averaging the simulated particles properties. In this case, only the aerodynamic properties are deemed of interest, specifically the aerodynamic forces and moments with respect to a fixed center of rotation.

For all the simulations in the current work, the collisions between particles and object's walls have been simulated with a mixed specular-diffusive reflective model with a diffusive energy accommodation assumed to be $\alpha_{diff} = 0.93$. The accommodation coefficient is a source of uncertainty which should be taken into account when performing aerodynamic simulations; as it has been thoroughly explained by Moe et ali,[14,15] α_{diff} is highly variable, mainly depending on the orbital parameters, object's materials, solar activity and temperature. The last two, along with the molecular composition and the free flow velocity have an influence on the molecular speed ratio (S_R, eq. 2):

$$S_R = \frac{V_\infty}{\sqrt{2RT_\infty}} \tag{2}$$

where V_∞ is the assumed satellite velocity, R is the specific gas constant, and T_∞ is the free flow temperature. As it was reported by Cook,[3] the S_R has a great impact over the drag, therefore it must be blocked during the C_F modeling phase.

When performing DSMC simulations, a mesh is initialized with a number of simulated particles, in this case representative of the atmospheric composition and properties at a predefined altitude of 500km. Usually, the mesh refinement level is based on the free flow mean free path[23] (λ), but in the FM regime, the minimum mesh cell size is chosen in order to properly estimating the averaged macroscopic flow field properties and to accurate modeling the object's surface. For all the performed DSMC simulations, the flow field was initialized with 40 particles per cells, which is representative of a high accuracy. The atmospheric properties were directly obtained from a reference MSISE00 database. The atmospheric properties of interest were the 5 species molecular densities (O, O_2, N, N_2, Ar) and the average atmospheric temperature ($T_\infty = 960K$). As it has been shown by Bailey,[1] another parameter that influences the computed C_D is the wall to free flow temperature ratio: T_{wall}/T_∞. In this work, a reference $T_{wall} = 300K$ has been used for all the simulations. The flow velocity has been fixed to 7600m/s, which in accordance with all the others properties leads to a molecular speed ratio equal $S_R = 7.66$.

For this work aims, few hundreds of simulations were expected to be performed for the different parameterized geometries; therefore, it had been required to build a general DSMC automated simulation interface which performs the following tasks: 1) Atmospheric Database and general inputs preprocessing; 2) the modification of the object's geometry according to the input parametrization; 3) mesh preprocessing definition and initialization; 4) initialization of the simulated particles properties; 5) initialization of the boundary conditions, and simulation control (e.g.: time step, averaging time frame, etc...); 6) particles, forces and moments convergence control; 7) post-processing and data management. Since the simulations were all performed on the ARCHIE-WeST high performance computer, an additional job management interface had to be coded in order to control the entire process.

3. Adaptive Derivative High Dimensional Model Representation

The AD-HDMR approach developed by Kubicek et all,[6] which has already been employed for performing uncertainty quantification and sensitivity analyses of GOCE,[4] has been used in this work for preliminarily evaluating the aerodynamic C_F surrogate models.

The AD-HDMR algorithm begins the initialization decomposing the N-Dimensional statistical domain, predefined in accordance to a set of input statistical distributions (e.g.: uniform distributions for α, β, and A_{ratio}). The algorithm selects the most influencing defined sub-domains, according to a procedure based on the HDMR-cut methodology. From those domains, the AD-HDMR performs a sampling for the next set of inputs to be tested. The function of interest is then evaluated with the selected inputs, it must be noted that in this specific case, the inputs are sent to the DSMC automated simulation interface. The DSMC block automatically performs a preprocessing of the given inputs, generates the mesh, and initializes the DSMC simulation. After the DSMC simulation has reached a user-defined level of convergence, the C_D is returned to the AD-HDMR algorithm as if it were the results of a function evaluation. After a an adaptive number of tested samples, the algorithm begins the creation of preliminary SMs used to evaluate the problem's statistical properties, defining which models best interpolates the sampled points via an adaptive interpolation, where the models are chosen from a given set of interpolants. When the process is properly converged from a statistical point of view, the algorithm provides the final sensitivity analysis results, the investigated property statistical distribution (e.g.: a probability histogram), and the SMs of "important" inputs and their interactions.

4. FOSTRAD

The Free Open Source Tool for Re-entry of Asteroids and Debris[10] (FOSTRAD) has been developed over the past few years to provide the scientific community with an accessible tool capable of performing low-fidelity aerodynamic and aero-thermodynamic simulations for re-entry scenarios. Initially, the tool had been specifically designed to study simple shaped objects representative of space debris and asteroids. This work focuses on the aerodynamic module, which is of essential interest when performing re-entry trajectories analysis and impact footprint estimation. FOSTRAD is a fast and efficient code that can be coupled with trajectory propagators and uncertainty analyses tool.[12]

Recently, FOSTRAD has been employed for studying the re-entry of different complex objects such as spacecraft and satellites.[2] A set of thorough tests on different geometries (e.g.: STS orbiter, GOCE, CFASTT-1 spaceplane) have highlighted the need of improving the tool and further develop additional preprocessing phases in order to increase the overall tool accuracy. The main idea behind this work is that it is possible to reduce the uncertainty on the aerodynamic performance, and then on the overall uncertainty on re-entry analyses, by introducing general or specific aerodynamic error reduction surrogate models.

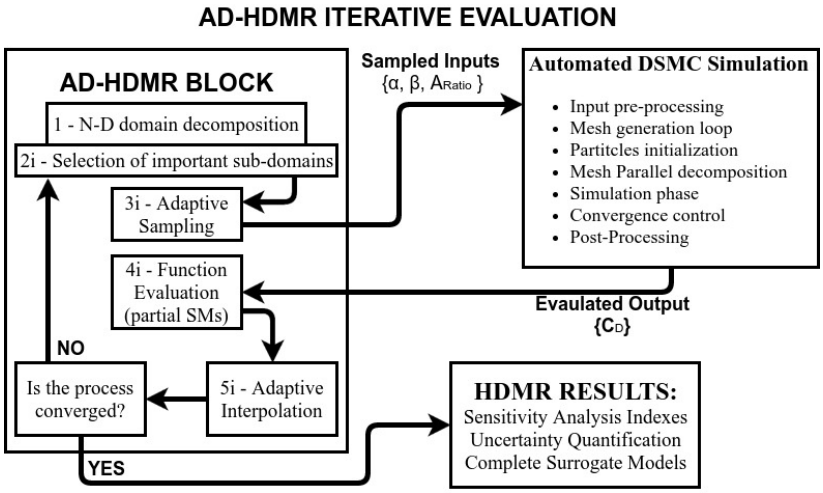

Figure 1: Iterative AD-HDMR process flow chart and DSMC coupling scheme: (1) The AD-HDMR starts decomposing the input domains. (2i) Selects the important sub-domains according to the latest results. (3i) Performs the adaptive sampling and requests a new DSMC simulation. (4i) Evaluates the function with respect to the sampled inputs. (5i) Adaptively selects an interpolation method. Performs the steps from 2i to 5i till the process has reached a statistical convergence.

4.1 Aerodynamics

FOSTRAD employs different simplified aerodynamic formulations for the different flow regimes. The flow regimes are characterized in accordance to their degree of rarefaction based on the Knudsen Number (Kn), defined as eq. 3

$$Kn = \frac{\lambda}{L} \tag{3}$$

where λ is the mean free path, and L is the characteristic length of the object. Where the higher continuum boundary limit is assumed at $Kn \leq 0.01$ and the FM regime can be assumed for $Kn \geq 10$. Within that range the flow is assumed to be in a rarefied transitional regime, where FOSTRAD uses a sigmoid bridging function based on the Kn.[10]

In the FM regime, FOSTRAD employs the Schaaf and Chambre model[22] for computing pressure and shear coefficients (respectively eq. 4 and eq. 5).

$$\begin{aligned} C_P = \frac{1}{S_R^2}\Bigg\{\Bigg(\frac{2-\sigma_N}{\sqrt{\pi}} S_R \sin\theta + \frac{\sigma_N}{2}\sqrt{\frac{T_w}{T_\infty}}\Bigg) exp\left[-(S_R \sin\theta)^2\right] \\ + \left[(2-\sigma_N)\left((S_R \sin\theta)^2 + \frac{1}{2}\right) + \frac{\sigma_N}{2}\sqrt{\frac{\pi T_w}{T_\infty}} S_R \sin\theta\right](1 + erf(S_R \sin\theta))\Bigg\} \end{aligned} \tag{4}$$

where C_P is the pressure coefficient, S_R is the molecular speed ratio as defined in eq. 2, σ_N is the normal energy accommodation coefficient, θ is the panel inclination angle with respect to the flow direction, and $erf()$ is the error function.

$$C_\tau = -\frac{\sigma_\tau \cos\theta}{S_R\sqrt{\pi}}\left\{exp\left[-(S_R \sin\theta)^2\right] + \sqrt{\pi}\, S_R \sin\theta\left[1 + erf(S_R \sin\theta)\right]\right\} \tag{5}$$

where C_τ is the tangential shear coefficient, and σ_τ is the tangential energy accommodation coefficient. By using this simplified approach, the forces acting on the surface of a body in a FM flow regime can be computed.

In the continuum regime, FOSTRAD uses the modified Newtonian theory proposed by Lees,[7] the tangential shear coefficient is neglected and the pressure coefficient is defined as in eq. 6

$$C_P = C_{P,max} \sin^2\theta \tag{6}$$

where the notation is the same as in the FM regime. It must be highlighted that these coefficients are computed for each of the panels composing the object's triangular mesh. The evaluation of the pressure and shear coefficients on

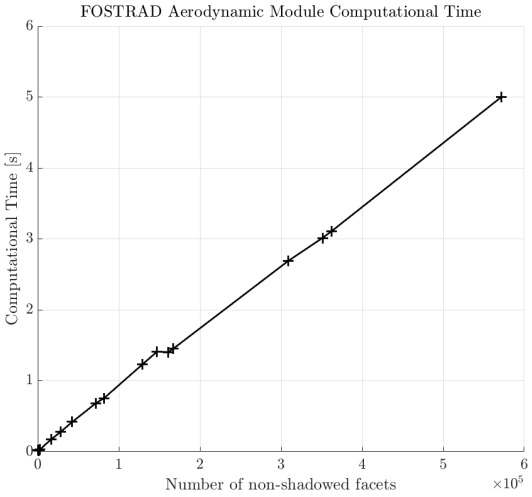

Figure 2: FOSTRAD aerodynamic module computational time escalation with the number of exposed triangular facets.

all the geometry's panels provides the macroscopic forces and moments acting on the object. Both models (FM and continuum) assume that for a shadowed (or leeward) panel, the pressure coefficient can be neglected.

4.2 FOSTRAD General Updates

Recently, FOSTRAD has been further developed to simplify its application, increase the computational efficiency, and improve the accuracy of both the aerodynamic and aero-thermodynamic modules. In addition, FOSTRAD can now be more easily interfaced with other codes, for studying trajectory propagation, performing uncertainty quantification or creating surrogate models; some examples will be shown in Section 6. With the recent computational improvements, FOSTRAD can simulate a single point aerodynamic properties in the continuum or FM regime in the order of ~0.1s, considering an average mesh with ~10'000 exposed triangles, on an average workstation equipped with an Intel® Core™ i7-4790 CPU 3.60GHz x8. When computing the properties in the transitional regime, FOSTRAD requires between 5 and 10 times the computational time of the single step. The aerodynamic computational time increases linearly with the number of detected facets (Figure 2). It must be highlighted that the number of facets depends on the complexity of the geometry and the desired accuracy, a number of facets within 2'000 and 20'000 is usually enough to simulate a complex geometry with a good accuracy.

4.3 Shadowed Panels Determination

Many different methods may be used to distinguish windward and leeward (or shadowed) triangular facets; according to the most common computer graphics rendering techniques: ray-tracing algorithms, depth-sorting algorithms, and back-face culling and occlusion culling.[24] The shadowed facets determination phase is essential as they have a negligible aerodynamic contribution, which is assumed to be zero. If the aerodynamic effect of shadowed facets were to be computed, the algorithm would compute a wrongly increased aerodynamic drag. Previously, FOSTRAD detected shadowed panels with an algorithm built on: 1) a back-face culling and 2) an occlusion culling-based technique: the *Pixelator*, initially described by Mehta.[11]

The back-face culling is a preprocessing phase commonly used in computer graphics rendering algorithms, which checks the polygons normal. If the angle between the polygon normal and the position vector pointing to the point of observation from the polygon barycenter is greater than ±90deg then the polygon is not rendered. Since the process is based on the computation of polygons normals, whose direction depends on the polygon winding direction (clockwise or counter-clockwise), if the winding direction is not consistent all over the mesh, there will more likely be inconsistency on normal directions; e.g. normals with opposite directions on a same flat face. Typically, this happens for complex objects with flat surfaces or after a re-elaboration of the unstructured mesh, i.e.: local mesh refinement. The problem leads to two possible cases: a) windward facets detected as "shadowed" panels, and therefore neglected on the aerodynamic computation and b) leeward facets detected as if they were facing the flow and therefore wrongly contributing to the aerodynamic forces. Both scenarios cause considerable errors on the aerodynamic forces and

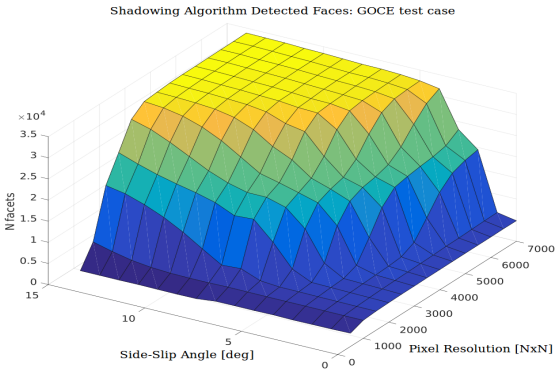

Figure 3: FOSTRAD panels shadowing algorithm convergence on the number of pixels and the attitude. Tested on the model of GOCE.

moments. Therefore, a method for correcting the normals' direction has been implemented and different consistency checks have been introduced.

The back-face culling role was mainly to reduce the number of facets to be elaborated during the *Pixelator* application. In the previous version of FOSTRAD, the back-face culling resulted in a decreased computational time of the shadowed panels determination phase. In the current version of FOSTRAD, the back-face culling module can be enabled or disabled according to the user needs. In fact, the radical recoding of the occlusion culling algorithm, makes the computational efficiency[2] advantage granted by the back-face culling not very significant. Therefore, it is recommended that for complex geometries the back-face culling algorithm is disabled.

The newly coded panel shadowing determination algorithm (based on the *Pixelator*) detects the shadowed facets (and non-) according to a sequence of operations: 1) assigns a unique 24-bit RGB color code to each facet; 2) plots and rotates the object according to the flow direction; 3) generates an RGB bitmap directly into the workspace; 4) the algorithm determines which facets color codes are present in the stored bitmap, these facets will be the non-shadowed ones. The algorithm has been improved in several ways:

1. The code has been completely vectorized, making the algorithm computationally insensitive to the mesh size
2. The algorithm automatically stores a bitmap, without taking a screen shot
3. Introduction of a convergence loop on the detected facets with an increasing pixel resolution

The code vectorization greatly improves the algorithm performance, the number of triangular facets does not sensibly influence the computational cost, making the previously used back-face culling preprocessing phase not required. The ability of storing the bitmap directly into the workspace grants a great improvement into the performance and the chance of creating bitmaps having pixel resolutions much higher than the display resolution (virtually limited only by the bitmap memory size on the RAM). This update allows the user to define the bitmap resolution to be used, which influences the number of detectable faces. A higher resolution grants a better precision, but also increases the computational cost. As shown in Figure 3, the number of detected facets depends on the object shape and attitude and the used pixel resolution. This led to the introduction of a convergence loop on the number of facets or, as an alternative, the detected facets' total area. The convergence loop may become very expensive depending on the object complexity, size of facets, and object attitude. Therefore, the user must reasonably choose the shadowing algorithm input parameters: 1) starting pixel resolution, 2) maximum pixel resolution (to avoid the RAM saturation), 3) pixel resolution step size, 4) maximum residual acceptable for the convergence on the number of facets or their total area.

In Figure 4 the color coding for the ellipsoid rotated according to the assumed flow direction (explicitly plotted for demonstration purposes) is shown on the left; on the right, the same ellipsoid has been used for benchmarking the computational times and the face convergence for a fixed attitude and a variable pixel resolution. It can be observed that attitudes and pixel resolutions greatly affect the ability of the shadowing algorithm to detect the correct number of faces. It must be highlighted that the faces that are left "undetected" or "wrongly-shadowed" are the ones with the highest inclination with respect to the flow direction, therefore, their contribution to the local aerodynamics are the lowest. As the computational time increases exponentially on the pixel resolution, a compromise between computational efficiency and aerodynamic accuracy must be sought.

With the new version of the shadowing algorithm, the user can also activate an adaptive refinement of the shadowed facets neighbors. This is required in order to obtain a better accuracy; in fact, the facets are shadowed only when

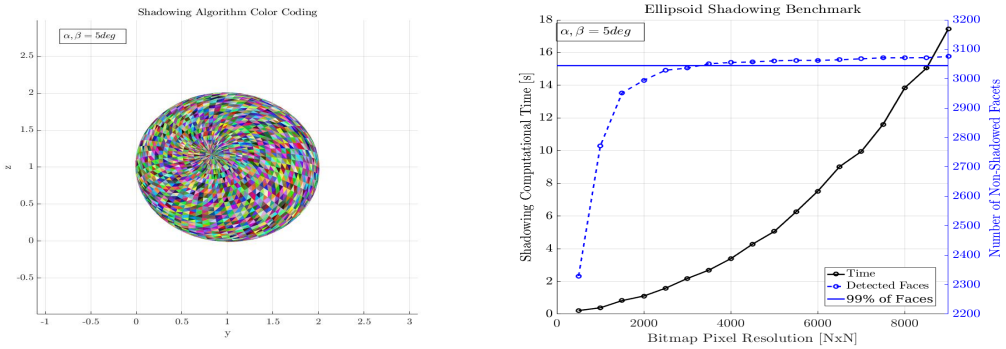

Figure 4: Shadowing computational time wrt pixel resolution. On the left: the ellipsoid geometry used for the test $\alpha, \beta = 5deg$. On the right: the number of non-shadowed facets convergence and the computational time for the 24-bit color coding.

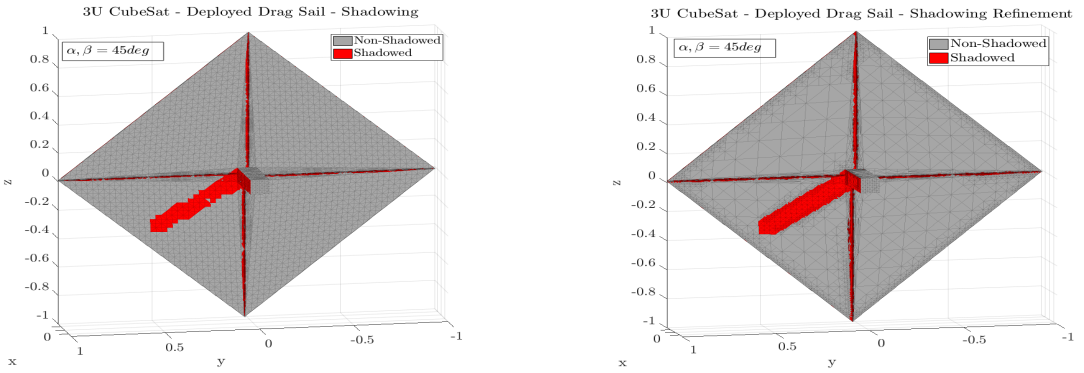

Figure 5: Shadowing application on the 3U CubeSat with deployed drag sail for $\alpha, \beta = 45deg$. On the left the standard shadowing, on the right: the shadowing with the adaptive mesh refinement.

they are completely hidden by other polygons. An example of the shadowing algorithm applied to the studied 3U CubeSat with the ARTICA drag sail system is shown in figure 5, on the left it is shown the result of a very fine mesh without the adaptive refinement, and on the right it is shown a coarse mesh with the use of the shadow adaptive refinement. It is observable how the shadow projected by the CubeSat main body is "discretized", and the actual shadowed area is less than the true projected area, as indeed, the facets are considered shadowed only when they are completely covered by other mesh triangles. Depending on the mesh refinement level, this could cause a variable error on the aerodynamic computations, which usually leads to an overestimation of the drag. The introduction of the adaptive mesh refinement on the shadowed facets will decrease the discrepancy between the real shadowed area and the discretized one, reducing the aerodynamic error. The adaptive shadow refinement is performed during the facets convergence loop, iteratively refining the shadowed facets border neighbors.

5. Methodology

In spite of the efforts for improving and correcting FOSTRAD's aerodynamic module, for non-hemispherical objects characterized by sharp edges and flat surfaces, FOSTRAD still shows a sensible error on the computed drag. The FM regime aerodynamic errors depend mainly on objects' lateral area and attitude. Therefore, for further improving the aerodynamic module, two different C_F SMs have been defined and tested. Although the C_F have been computed only for the FM regime, the corrections will also improve the results within the transitional regime, which are based on the bridging function between the FM and the continuum regime.

The C_F SM have been defined for two different kind of geometries: parallelepiped and cylinders. The geometries have been parameterized based on the front area to total area ratio:

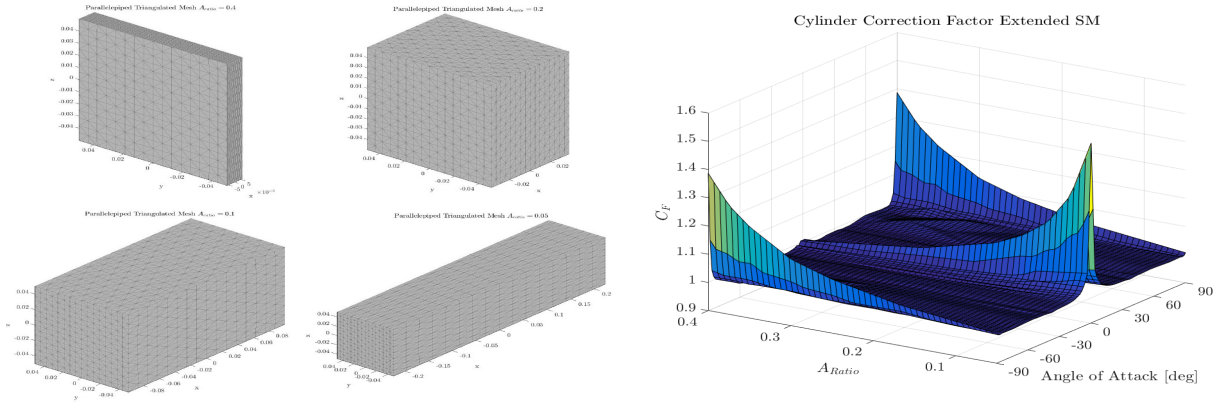

Figure 6: On the left: parallelepiped parameterization based on the A_{ratio}. On the right: cylindrical geometry C_F surrogate model.

Table 1: Configurations evaluated for the C_F.

Case	A_{ratio}	α	β
Parallelepiped	[0.05; 0.4]	[0; 90]	[0; 90]
Cylinder	[0.05; 0.4]	[0; 90]	-

$$A_{ratio} = \frac{A_{ref}}{A_{tot}} \tag{7}$$

where A_{ref} for the parallelepiped has been fixed to $A_{ref,p} = 0.01m^2$ (equivalent to a parallelepiped with a square frontal face of side 0.1m) and for the cylinder $A_{ref,c} = \pi(0.1/2)^2$ $[m^2]$. It is interesting to highlight that when $A_{ratio} = 0.1\overline{6}$ the geometries are cubic, and that the parallelepiped parameterization covers the different CubeSats configurations (Figure 6 on the left). As long as the aerodynamics are computed within the FM regime, the scale of the object is not relevant, therefore, the C_F are applicable to different scaled objects. In addition, they would be usable also for similar shaped geometries, e.g.: GOCE geometry resembled a cylinder with two big fins, therefore, the cylindric C_F would be usable for that geometry.

The ranges of analyzed parameters are reported in Table 1. For the symmetric nature of the analyzed geometries, it will be possible to extend the use of the C_F to wider attitudes. The area ratio has been chosen to stay within the boundary limits of a finite length geometry and "not-flat-plate" cases. The infinite length cylinder or parallelepiped and the flat-plate case would be equivalent to a $A_{ratio} \to 0$ and $A_{ratio} \to 0.5$ respectively. This two cases have not been presented here because they would need a specific implementation on the DSMC side with a subdivision of the attitude ranges and their application would be limited to extreme cases.

The preliminary C_F models were built using the the integrated approach of the AD-HDMR controlling the DSMC automated interface and FOSTRAD. Both the software used the atmospheric inputs listed in Section 2, in this way the atmospheric variables were blocked, thus the C_F takes into account only the variation due to the attitude and the shape. The AD-HDMR built the dataset to be used by the surrogate model generation phase directly computing the C_F.

The preliminary SM evaluation performed via the AD-HDMR identified that all the considered variables and their interaction were significant. Therefore, the parallelepiped correction factor surrogate model ($\mathbb{C}_{F,p}$) was built as the combination of three 1st-order models, three 2nd-order interactions, and one 3rd-order interaction. Meanwhile, the ($\mathbb{C}_{F,c}$) was defined by 3 models: two 1st order models and one 2nd order interaction. The preliminary S.M. interpolation datasets defined by the AD-HDMR have been thoroughly analyzed and locally refined to increase the SM accuracy. The parameterized cylindrical $\mathbb{C}_{F,c}$ is shown in Figure 6 on the right. An example of the N-Dimensional $\mathbb{C}_{F,p}$ is shown in Figure 7 for two different side-slip iso-surfaces respectively at 0deg and 90deg. The surrogate models have been defined using a different interpolation methods: 1-D Piecewise Hermitian Cubic Interpolation, polynomial and linear N-D interpolation.

The created drag coefficient $\mathbb{C}_F$ has been used to perform a Monte Carlo analysis for both geometries. The

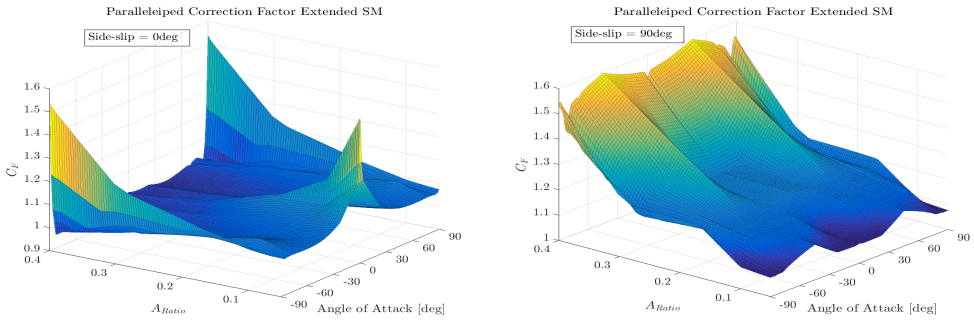

Figure 7: Parallelepiped C_F surrogate models for two different constant side-slip angles 0deg (on the left) and 90deg (on the right). It is possible to notice the strong interaction between all different variables taken into consideration.

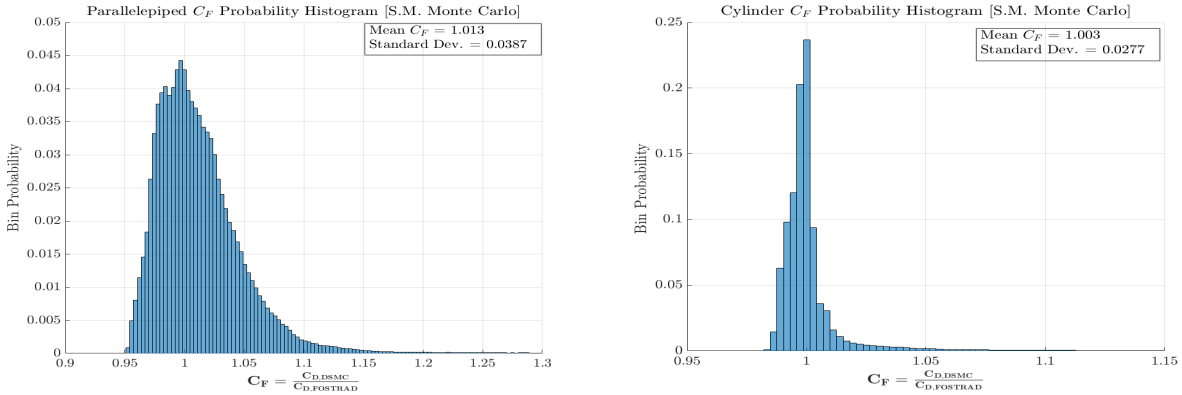

Figure 8: Monte Carlo analysis results on the drag $\mathbb{C}_F$, representative of the average random tumbling discrepancy between FOSTRAD and the DSMC code. The parallelepiped and cylinder are shown on the left and the right respectively.

results are shown in Figure 8; the analyses are representative of the statistical discrepancy between FOSTRAD and the DSMC for the parameterized geometries. Assuming a random tumbling attitude, the average DSMC-to-FOSTRAD error would be very low. It must be highlighted that the SM are subject to minor errors due to the used interpolation techniques and accuracy, thus the errors could be higher (or lower), but the results are representative of the random tumbling aerodynamic drag error magnitude.

6. Correction Factors Surrogate Models Test Cases

In order to test and verify the surrogate models application and accuracy, three different test cases have been considered:

1. Comparative aerodynamic analysis (drag, lift, and pitching moment coefficients) of a set of inputs simulated using both codes DSMC and FOSTRAD on both geometries (with and without C_F)
2. Aerodynamic analyses of a drag sail system implemented in a 3U CubeSat (ARTICA system)
3. GOCE C_D analysis during the drag-free orbital phase at ~260km, using a previously built DSMC C_D SM[4]

6.1 Cylinder and Parallelepiped Correction Factor Tests

In order to test the validity of the created C_F SMs, a set of tests have been carried out on both geometries. As the SMs have been defined according to a finite number of sampling points, the models are expected to present a higher error when they are used far from the sampled points. For this reason, arbitrarily chosen intervals have been analyzed,

comparing the FOSTRAD corrected $\mathbb{C}_F$ with DSMC results. Numerous test have been performed for different α, β, and A_{ratio}. For the sake of brevity, only some of the most significant results have been chosen to be presented.

In Figure 9 the corrected FOSTRAD C_D for a parallelepiped (on the left) and a cylinder (on the right) are shown. For the parallelepiped, the raw FOSTRAD results are underestimating the actual C_D, while the corrected model presents some discrepancy for low angles of attack. This is due to the interpolation techniques used for building the SMs and the limited number of used points. Using a better refined sampling database would provide more accurate SMs. For the cylinder, FOSTRAD simulations show a underestimation at both low and high angles of attack, while the corrected version greatly reduces this error. For intermediate attitudes, FOSTRAD does not present a sensible discrepancy, as it would have been expected considering that the lateral cylindrical surface has a hemispheric shape.

The analyses have been performed also for the lift and pitching moment coefficients (C_L and $C_{M,z}$ respectively). The $C_{M,z}$ has been analyzed with a reference center of rotation (CofR) chosen to be at the center of the backward face for each parametrized case; $CofR = [X_{b,f}\ 0\ 0]$, where $X_{b,f}$ is the x position for the backward face. The C_L analyses have shown that FOSTRAD slightly overestimates the lift when the geometries are at a low angle of attack (Figure 10). By observing the results, and considering the mathematical challenges for defining a C_L when the coefficients are very low ($C_L \to 0$), it was decided not to apply any correction to the lift. A different approach could be proposed by observing the trend for the two geometries: running two FOSTRAD simulations at $\alpha = 0deg$ and $\alpha = 10deg$ and linearly interpolating between the obtained C_L values. This would make the computation of the lift slightly more accurate, but also twice as expensive, therefore this approach would be usable only when an accurate C_L is required; in addition, this approach would definitely be case dependent.

Taking into consideration the moments shown in Figure 11, it is possible to observe that FOSTRAD estimates the cylinder $C_{M,z}$ very accurately. Although, analyzing the moments for parallelepipeds it is evident that they show the same underestimation highlighted for the drag. Applying the drag C_F the underestimation and the average error is greatly reduced.

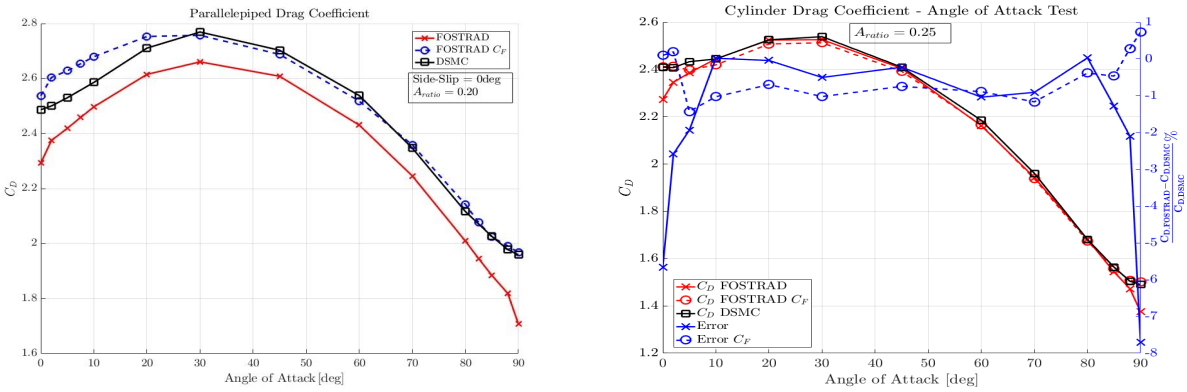

Figure 9: FOSTRAD-DSMC C_D comparisons for parallelepipeds (on the left) and cylinders (on the right).

6.2 ARTICA Deployed Drag Sail Aerodynamic Analysis

ARTICA is an autonomous deorbiting system designed to be compliant with the CubeSat class of nanosatellites end-of-life disposal regulations. The main design driver was to ensure the respect of IADC guidelines for all common CubeSat orbits in a compact form factor aiming at limiting the impact on the satellite. The ARTICA system was designed to be installed onto a CubeSat to work as a stand alone device, and provide its complete functionality even in the case of the main satellite failure. In fact, the device is already equipped with a proper power system, electronics, deployment switches and remove before flight badge. In order to enhance reliability, ARTICA control circuit is characterized by the redundancy of critical electronic components. In the standard configuration ARTICA automatically deploys a $2.1m^2$ drag sail after a preset amount of time (up to 3 years after launch separation); alternatively the opening of the sail can be prompted by the main satellite.

The first version of the system is shown in Figure 12 on the left: in a closed configuration the system is characterized by a volume of 30x100x100mm. ARTICA system and fit check integration on a mock-up 3U CubeSat is shown in Figure 12 (center). The system has undergone environmental qualification campaign (vibration, thermo-vacuum), followed by opening tests to assess the full functionality. The system first launch is scheduled for June 2017, where ARTICA constitutes one of the payloads of URSA MAIOR, the 3U Cubesat developed by the University of Rome "La

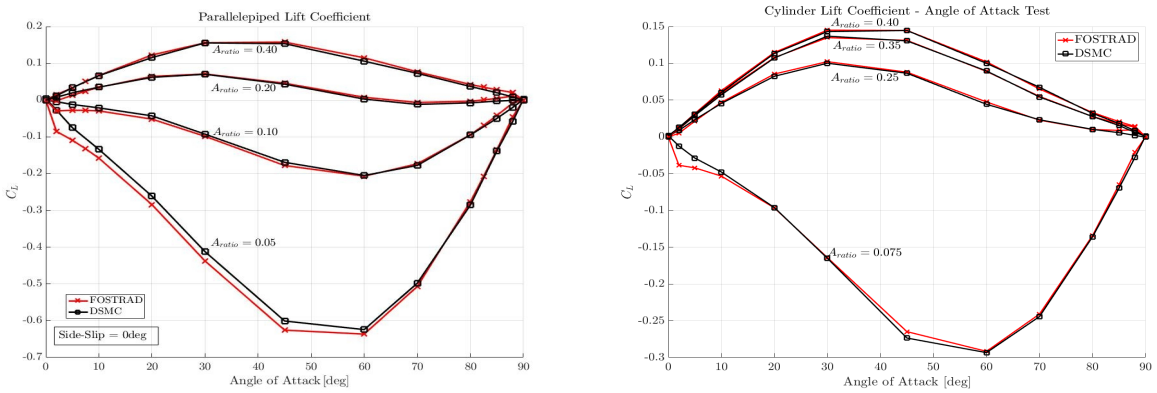

Figure 10: FOSTRAD-DSMC C_L comparisons for parallelepipeds (on the left) and cylinders (on the right). No correction has been applied to the C_L.

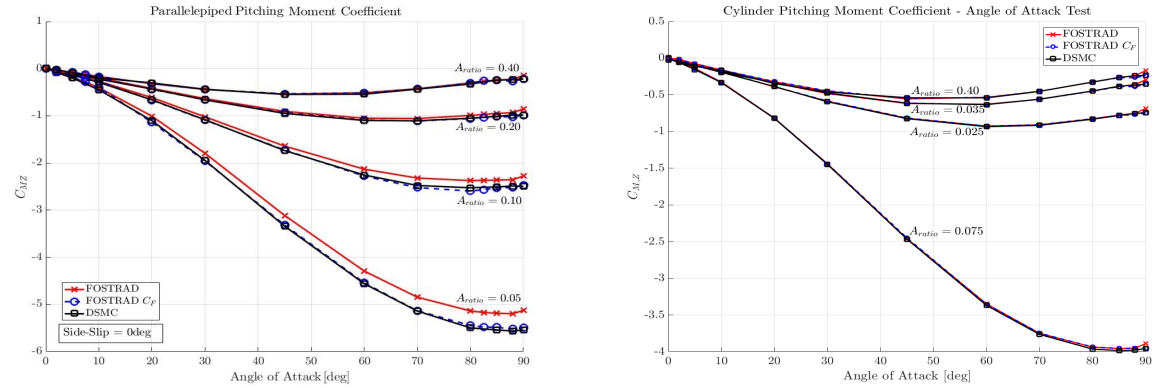

Figure 11: FOSTRAD-DSMC $C_{M,z}$ comparisons for parallelepipeds (on the left) and cylinders (on the right). The same drag $\mathbb{C}_F$ has been applied to the moments, the corrected models show a very accurate agreement.

Sapienza" in the frame of QB50 mission: an international network of 2U and 3U CubeSats whose main goal is the in situ and multi-point collection of measurements in the lower thermo-sphere and in-orbit technologies functionality demonstration. URSA MAIOR will be placed in a 500 km SSO: eleven months after the in orbit injection, ARTICA on board electronics will trigger the opening mechanism and deploy the sail. In order to monitor orbital decay and compare with analysis results, system performances will be monitored and evaluated by means of orbital data sent from the 3U satellite and/or from available TLE. A new version of ARTICA is under development to be compatible also with the 6U CubeSats class: it is characterized by a more compact volume (up to 20x90x90mm) that can be customized to adapt to all commercially available structures, while keeping the same nominal surface area. The 3D model used for the aerodynamic analysis is shown in Figure 12 on the right.

The aerodynamic analyses performed on the 3U CubeSat were mainly focused on the drag coefficient, as the main objective of the ARTICA system was to increase the orbital decay rate. In order to assess the drag increment achieved by the drag sail deployment the two configuration have been tested. The simulations have been performed by coupling both DSMC and FOSTRAD to the AD-HDMR algorithm. The 3U CubeSat with the closed sail, whose model was equivalent to a parallelepiped with a volume of 340x100x100mm, has been evaluated using uniform distributions of the following parameters: $S_R = [7.74; 9.46]$, $T_{wall} = [270; 300]K$, $\sigma_{diff} = [0.9; 1.0]$, $\alpha = [-90; 90]deg$, $\beta = [-90; 90]deg$; this distributions are representative for an object orbiting in a LEO with a random tumbling attitude. The results are shown on the left of Figure 13. In the same figure (on the right), are shown the results for the simulations of the system with the deployed drag sail by assuming the random tumbling motion.

Analyzing the pitching and yawing moment coefficients (Figure 14), which were obtained assuming a center of gravity at the volumetric center of the closed system, it was possible to deduce that the satellite would eventually reach a stable attitude with the main CubeSat body in front of the drag sail. By running the previously generated C_D SMs

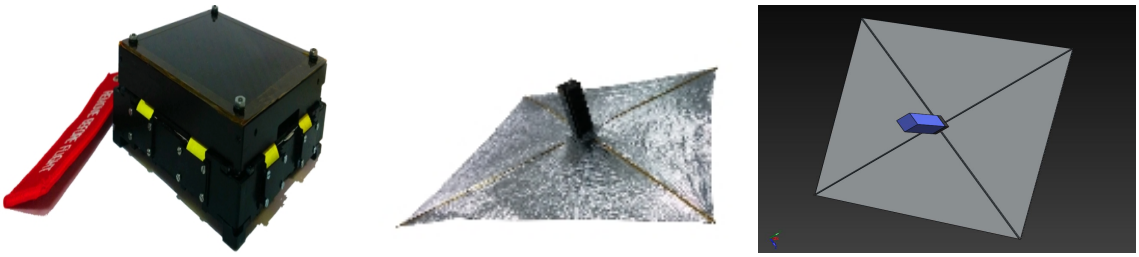

Figure 12: From the left to the right respectively: ARTICA closed system, ARTICA deployed drag sail, and 3U CubeSat with deployed drag sail 3D model.

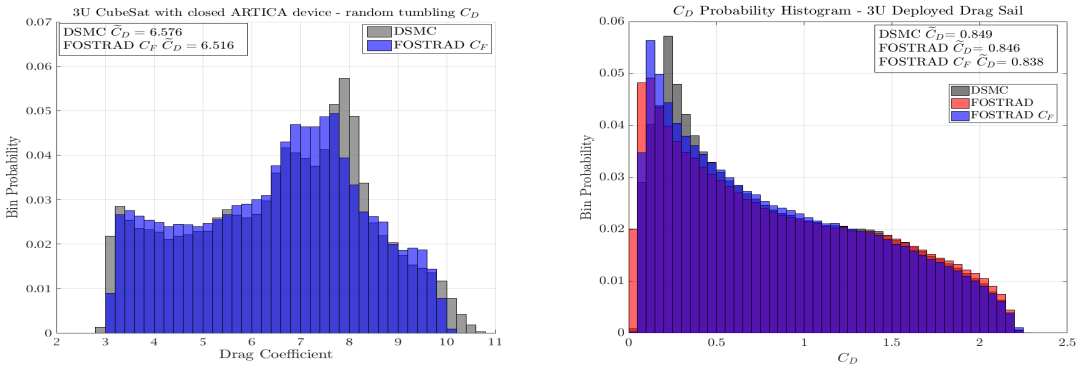

Figure 13: On the left: C_D probability histograms of the CubeSat with closed drag sail system. On the right: C_D probability histograms of the CubeSat with deployed drag sail. Both distributions have been obtained via the AD-HDMR-DSMC and AD-HDMR-FOSTRAD assuming a random tumbling attitude.

it was possible to obtain a more representative drag probability distribution. Assuming a tumbling around the x-axis with a uniform α and β distribution within [-10; 10]deg. The obtained C_D distribution is shown in figure 15, which is in agreement with the C_D commonly assumed for deployed drag sails, with a $\widetilde{C}_D = 2.13$. In addition, it is interesting to show also the C_D variation due to the attitude (Figure 15). The application of the C_F, in this specific case, does not provide any sensible improvement, even though the C_D distribution for the stabilized attitude has been slightly improved.

Comparing the results for the two possible configuration: a) the random tumbling CubeSat ($\widetilde{C}_{D,a} = 6.58$ and $A_{ref,a} = 0.01m^2$) and b) the deployed sail configuration with a stable attitude ($\widetilde{C}_{D,b} = 2.13$ and $A_{ref,b} = 2.1m^2$), at same orbital condition the drag gain is the following:

$$\widetilde{D}_b = \widetilde{D}_a \frac{\widetilde{C}_{D,b} A_{ref,b}}{\widetilde{C}_{D,a} A_{ref,a}} \approx 68\ \widetilde{D}_a \tag{8}$$

where $\widetilde{D}_b$ and $\widetilde{D}_a$ are the average drags for the two different closed and open drag sail configurations. In the first period after triggering the drag sail deployment, the satellite will keep random tumbling till it reaches a stabilized attitude; during this period the average drag gain will slowly increase from ~27 to 68. The lower boundary has been computed with the random tumbling averaged DSMC $C_D = 0.85$ shown in Figure 13 on the right.

6.3 GOCE Drag Coefficient test case

The study on GOCE has been deemed as a good benchmark for testing the cylindrical $\mathbb{C}_F$. In fact, the complex and elongated shape of GOCE (Figure 16), makes it an interesting case for testing FOSTRAD's panel method application. Previously performed analyses had shown a considerable discrepancy between the C_D computed via FOSTRAD and DSMC,[2] therefore, testing C_F application would provide useful information to understand whether or not is it possible to apply the corrective factors to similar shapes and geometries. Indeed, GOCE's main body could be easily simplified with a cylindrical body with two big fins.

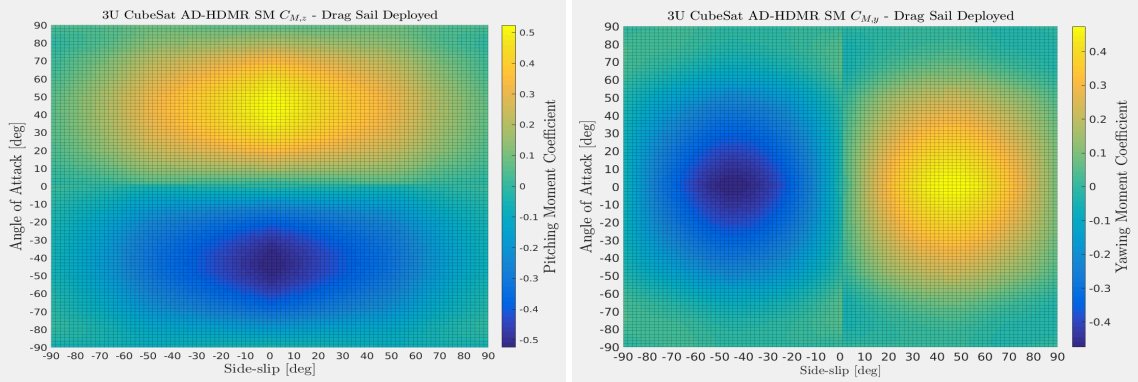

Figure 14: Pitching and Yawing moment coefficients of the CubeSat with deployed drag sail obtained with AD-HDMR-DSMC analyses

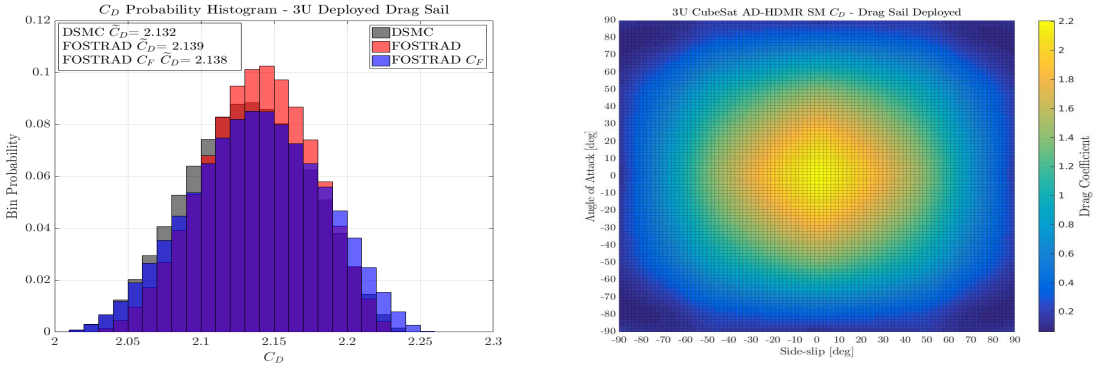

Figure 15: On the left: C_D for the 3U CubeSat with deployed drag sail assuming a stabilized attitude. On the right: the C_D variation over α and β, obtained with the AD-HDMR-DSMC SM.

In order to test the accuracy of the cylindrical $\mathbb{C}_F$, a previously defined C_D DSMC SM[4] has been compared to a Monte Carlo sampling performed via FOSTRAD with and without the correction. The C_D DSMC SM was defined for a broad range sensitivity analyses of GOCE aerodynamics in the FM regime considering 5 different parameters within the respective ranges: $S_R = [8; 12]$, $T_{ratio} = [0.01; 1.5]K$, $\sigma_{diff} = [0.5; 1.0]$, $\alpha = [-5; 5]deg$ and N_2 atomic density (which as long as the flow is in a FM regime resulted negligible). Using uniform distributions and the same 4500 samples for both DSMC and FOSTRAD, the results of the Monte Carlo sampling is shown in Figure 16 on the right. Observing the figure it is possible to notice that the cylindric C_F application greatly improves FOSTRAD accuracy. It must be reminded that the side-slip angle interval used for the sampling is very challenging for local panel inclination methods. Even though the corrected C_D distributions still present a lower tail, the average C_D has been greatly improved. In fact, FOSTRAD without correction underestimates the C_D of a ~18%, whereas the corrected values show just a minor discrepancy.

7. Conclusions

A thorough comparison between high-fidelity (DSMC) and low-fidelity (FOSTRAD) hypersonic free molecular aerodynamic analyses have been carried out, highlighting where the highest discrepancy lies. The highest differences are shown on elongated shapes (low $A_{ratio}/A_{tot} \to 0$) with flow direction parallel to the longitudinal axis, and thin geometries (e.g.: flat plates, $A_{ratio}/A_{tot} \to 0.5$) with flows impacting from the short side. The cylindrical shapes have shown a sensible error only on the drag coefficient, whereas parallelepipeds have shown a sensible underestimation on the drag and pitching moment coefficients.

The latest updates of FOSTRAD have been presented and thoroughly tested, highlighting the computational efficiency and the tool integrability within other frameworks (e.g.: interfacing FOSTRAD and the AD-HDMR for

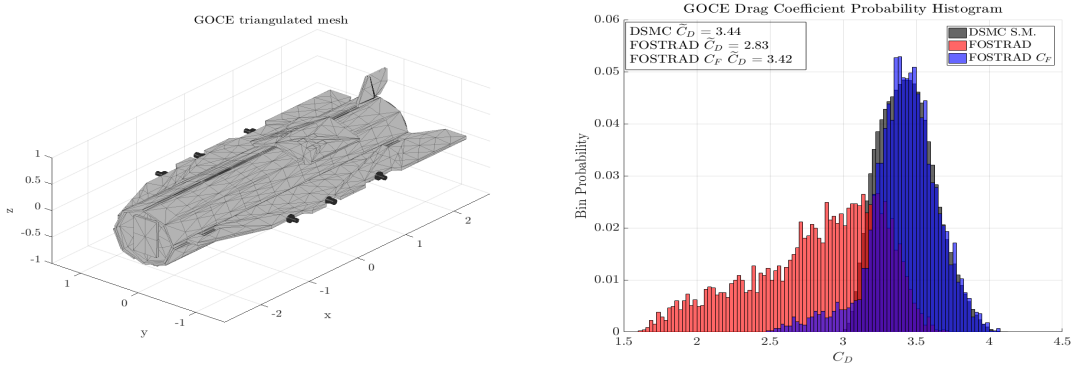

Figure 16: On the left: GOCE triangulated mesh used for FOSTRAD simulations. On the right: Monte Carlo probability distribution (4500samples) of a DSMC predefined SM and FOSTRAD with and without C_F

.

performing uncertainty quantification and sensitivity analysis or surrogate modeling).

Two different surrogate models (SM) of drag corrective factors (C_F) have been generated and implemented in FOSTRAD. The SM's have shown a good applicability also on likely-shaped geometries (e.g.: the application of the cylindrical C_F on GOCE test case or the 3U CubeSat with ARTICA deployed drag sail), greatly reducing FOSTRAD errors. The developed C_F provide the software with an improved aerodynamic accuracy, and then will reduce FOSTRAD uncertainty when simulating spacecraft, satellite and debris re-entry scenarios, allowing for a better estimation of the ground risk.

Moreover, a set of aerodynamic analysis of the URSA MAIOR 3U CubeSat (part of the QB50 project) with the installed ARTICA drag sail system have been performed. The results have shown that the use of a $2.1m^2$ drag sail could augment the average drag acting on the satellite up to 68 times.

Considering the successful test applications of the correction factors, in the future it is expected to further develop FOSTRAD, building C_F for more geometries. In addition, the currently implemented C_F will be further refined to grant a better accuracy and reliability.

8. Acknowledgments

The authors would like to state that the results were obtained using the EPSRC funded ARCHIE-WeSt High Performance Computer (www.archie-west.ac.uk). EPSRC grant no. EP/K000586/1.

References

[1] AB Bailey and J Hiatt. Sphere drag coefficients for a broad range of mach and reynolds numbers. *Aiaa Journal*, 10(11):1436–1440, 1972.

[2] G Benedetti, V Nicole, E Minisci, A Falchi, and M Vasile. Low-fidelity modelling for aerodynamic characteristics of re-entry objects. In - *To be published in the Proceedings of the Stardust Final Conference: Advances in Asteroids and Space Debris Engineering and Science, Springer*, 2016.

[3] GE Cook. Satellite drag coefficients. *Planetary and Space Science*, 13(10):929–946, 1965.

[4] A. Falchi, E. Minisci, M. Kubicek, M. Vasile, and S. Lemmens. Hdmr-based sensitivity analysis and uncertainty quantification of goce aerodynamics using dsmc. In - *To be published in the Proceedings of the Stardust Final Conference: Advances in Asteroids and Space Debris Engineering and Science, Springer*, 2016.

[5] G Koppenwallner, B Fritsche, T Lips, and H Klinkrad. Scarab-a multi-disciplinary code for destruction analysis of space-craft during re-entry. In *Fifth European Symposium on Aerothermodynamics for Space Vehicles*, volume 563, page 281, 2005.

[6] M Kubicek, E Minisci, and M Cisternino. High dimensional sensitivity analysis using surrogate modeling and high dimensional model representation. *International Journal for Uncertainty Quantification*, 5(5), 2015.

[7] L Lees. Hypersonic flow. In *Fifth International Aeronautical Conference (Los Angeles, Calif*, pages 241–276, 1955.

[8] T Lips and B Fritsche. A comparison of commonly used re-entry analysis tools. *Acta Astronautica*, 57(2):312–323, 2005.

[9] CE Martin, JE Cheeses, N Sanchez-Ortiz, H Klinkrad, K Bunte, S Hauptmann, B Fritsche, and T Lips. Introducing the esa drama tool. *Science and Technology Series*, 110:219–233, 2005.

[10] P Mehta, E Minisci, M Vasile, A C Walker, and M Brown. An open source hypersonic aerodynamic and aerothermodynamic modelling tool. In *8th European Symposium on Aerothermodynamics for Space Vehicles*, 2015.

[11] P M Mehta, G B Arnao, D Bonetti, E Minisci, and M Vasile. Computer graphics for space debris. In *Proceedings of the 6th International Conference on Astrodynamics Tools and Techniques, Darmstadt, Germany*, pages 14–17, 2016.

[12] P M Mehta, A Walker, M Brown, E Minisci, and M L Vasile. Sensitivity analysis towards probabilistic re-entry modeling of spacecraft and space debris. In *AIAA Modeling and Simulation Technologies Conference*, page 3098, 2015.

[13] J Merrifield, J Beck, G Markelov, and R Molina. Simplified aerothermal models for destructive entry analysis. In *8th European Symposium and Aerothermodynamics for Space Vehicles*, 2015.

[14] K Moe and M M Moe. Gas–surface interactions and satellite drag coefficients. *Planetary and Space Science*, 53(8):793–801, 2005.

[15] K Moe, M M Moe, and S D Wallace. Improved satellite drag coefficient calculations from orbital measurements of energy accommodation. *Journal of spacecraft and rockets*, 35(3):266–272, 1998.

[16] P Omaly and M Spel. Debrisk, a tool for re-entry risk analysis. In *ESA Special Publication*, volume 699, 2012.

[17] J. N. Opiela, E. Hillary, D. O. Whitlock, and Hennigan M. Debris assessment software, user guide. Technical report, NASA Lyndon B. Johnson Space Center, January 2012.

[18] WC Rochelle, JJ Marichalar, and NL Johnson. Analysis of reentry survivability of uars spacecraft. *Advances in Space Research*, 34(5):1049–1054, 2004.

[19] Wm C Rochelle, R E Kinsey, E A Reid, R C Reynolds, and N L Johnson. Spacecraft orbital debris reentry: Aerothermal analysis. 1997.

[20] T. J. Scanlon, E. Roohi, C White, M. Darbandi, and J. M. Reese. An open source, parallel dsmc code for rarefied gas flows in arbitrary geometries. *Computers And Fluids*, 39(10):2078–2089, 2010.

[21] T J Scanlon, C White, M K Borg, R C Palharini, E Farbar, I D Boyd, J M Reese, and R E Brown. Open-source direct simulation monte carlo chemistry modeling for hypersonic flows. *AIAA Journal*, 53(6):1670–1680, 2015.

[22] Samuel Albert Schaaf and Paul L Chambré. *Flow of rarefied gases*. Number 8. Princeton University Press, 1961.

[23] Zhi-Xin Sun, Zhen Tang, Ya-Ling He, and Wen-Quan Tao. Proper cell dimension and number of particles per cell for dsmc. *Computers & Fluids*, 50(1):1–9, 2011.

[24] H Zhang. Effective occlusion culling for the interactive display of arbitrary models. 1998.